Echo-assisted impulsive alignment of room-temperature acetone molecules

Junyang Ma,[1,2] L. H. Coudert,[4] F. Billard ●,[1] M. Bournazel,[1] B. Lavorel,[1] Jian Wu,[2,3] G. Maroulis,[5]
J.-M. Hartmann,[6] and O. Faucher ●[1]

[1]*Laboratoire Interdisciplinaire CARNOT de Bourgogne Franche-Comté,*
UMR 6303 CNRS-Université de Bourgogne, BP 47870, 21078 Dijon, France
[2]*State Key Laboratory of Precision Spectroscopy, East China Normal University, Shanghai 200241, China*
[3]*Collaborative Innovation Center of Extreme Optics, Shanxi University, Taiyuan, Shanxi 030006, China*
[4]*Institut des Sciences Moléculaires d'Orsay (ISMO), CNRS, Université Paris-Sud,*
Université Paris-Saclay, F-91405 Orsay, France
[5]*Department of Chemistry, University of Patras, GR-26500 Patras, Greece*
[6]*Laboratoire de Météorologie Dynamique/IPSL, CNRS, École polytechnique,*
Institut polytechnique de Paris, Sorbonne Université,
École Normale Supérieure, PSL Research University, F-91120 Palaiseau, France

We experimentally and theoretically investigate the field-free alignment of the asymmetric-top acetone molecule. Our study shows that the production of postpulse aligned molecules in dense samples (0.05–0.2 bar) of room-temperature acetone using a single-pulse excitation can be significantly improved by rotational alignment echoes induced in a two-pulse excitation scheme. We report the observation of fractional echoes that can be used to reveal the nonlinearity of the molecular system. In a proof-of-principle experiment, a prealigned sample of acetone is also used for third-harmonic generation. The analysis of the experimental data with numerical simulations based on quantum and classical models enables the determination of the collisional decay rate of acetone alignment, as well as a test of the static, second-order, electric hyperpolarizabilities of the molecule derived from *ab initio* calculations presented in this work.

I. INTRODUCTION

The alignment of molecules, an efficient way to overcome the random spatial distribution of molecular axes, is at the heart of many physical and chemical processes with multiple ramifications in the generation of high-harmonic radiations [1–3], molecular orbital tomography [4,5], collisional dissipations [6–8], and air lasing [9], to name but a few. In the last two decades, intense femtosecond laser pulses have successfully served as a powerful tool for achieving impulsive field-free molecular alignment of various molecules, which has led to a better understanding of rotational dynamics driven by strong laser fields [10–12]. Particular attention has been paid to linear and symmetric-top molecules thanks to their highly symmetrical structure allowing the achievement of a significant degree of alignment and a fully tractable numerical modeling. Controlling the rotation of asymmetric-top molecules is much more attractive given the wide variety of potential applications in chemistry and biology. Rotational dynamics of such molecules have

been extensively studied in the low-field regime by ultrafast coherence spectroscopy [13,14]. In order to understand and steer the rotation of asymmetric-top molecules exposed to a strong laser field, several works have experimentally and theoretically studied the short-pulse alignment of near-symmetric-top molecules with Ray's parameter κ close to ± 1 (with $\kappa = -1$ and $+1$ for prolate and oblate symmetric-top, respectively), such as SO_2 ($\kappa = -0.942$) [3,15–19], C_2H_4 ($\kappa = -0.914$) [15,20,21], 1,3-butadiene ($\kappa = -0.978$) [22], iodobenzene ($\kappa = -0.965$) [23,24], pyrimidine ($\kappa = -0.869$) [25], 3,4-dibromothiophene ($\kappa = -0.987$) [26,27], and the chiral propylene oxide molecule ($\kappa = -0.879$) [28].

However, many phenomena in nature involve complex polyatomic molecules structurally more asymmetric, i.e., with Ray's parameters closer to zero, which are more difficult to align than the previous category due to an increased lack of regularity of their rotational spectrum. In fact, field-free molecular alignment is closely linked to the molecules' ability to rephase their rotational coherences once stimulated by the laser pulse. The commensurability of the rotational energies of symmetric-top molecules is reflected in the time domain by a pattern of quasiperiodic quantum revivals which vanish at long time [29]. Conversely, the incommensurability of the rotational energies of asymmetric-top molecules leads to fast decreasing alignment revivals. In this context the present work reports the observation of field-free alignment
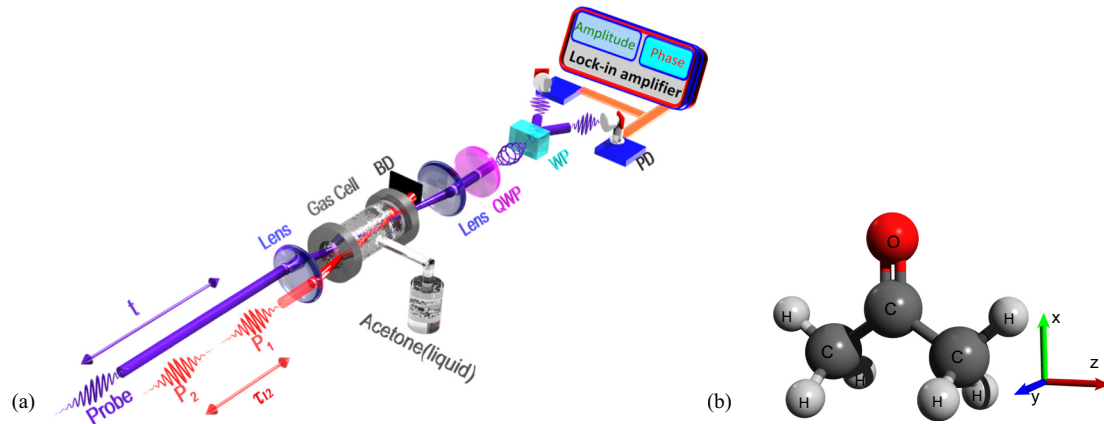
FIG. 1. (a) Experimental setup of the rotational alignment echoes produced by two ultrashort laser pulses $\mathcal{P}_1$ and $\mathcal{P}_2$ (800 nm) time-delayed by τ_{12}. The molecular alignment is probed by a third ultrashort laser pulse (400 nm). BD: beam dump, PD: balanced photodiodes, WP: Wollaston prism, QWP: quarter-wave plate. (b) The C_{2v} configuration used in both theoretical simulations. The body fixed xyz axis system is attached to the molecule using the I^r representation. For clarity its origin is not drawn at the molecular center of mass.

of gas phase acetone which, unlike the previously mentioned molecules, is oblate and highly asymmetric as evidenced by a small positive $\kappa = 0.37$. The revivals induced by a single pulse were studied first. As they turned out to be very weak under the present experimental conditions (room temperature and a pressure close to the saturation vapor pressure), an enhanced alignment signal was obtained using the rotational alignment echo based on a bi-pulse sequence excitation [30]. Fractional echoes resulting from the nonlinear geometry of the molecule could be observed for the first time in a probe-phase sensitive detection of molecular alignment. Among the possible applications, a sample of aligned acetone was then used in a nonlinear process to generate the third-harmonic radiation of a circularly polarized fundamental laser pulse.

II. ALIGNMENT OF ACETONE

A. Experimental setup

In the first part of this study, the aligned molecules are detected through the femtosecond time resolved birefringence setup depicted in Fig. 1(a). The molecules are impulsively aligned along the electric field of a short and intense linearly polarized laser pulse $\mathcal{P}_1$ (800 nm, 100 fs, 1 kHz) which is focused in a static gas cell that can be filled by evaporating liquid acetone. The resulting reorientation of the molecular axes induces a birefringence in the gas medium that is subsequently characterized by a time delayed weak probe pulse (400 nm) polarized at $45°$ with respect to $\mathcal{P}_1$. The former beam intersects, with a small angle, the pump beam at focus. The modification of the probe polarization is analyzed with a highly sensitive balanced detector providing a signal proportional to the alignment factor (see below). Rotational alignment echoes are produced by introducing a second 800 nm pump pulse $\mathcal{P}_2$, sharing the same polarization and propagation direction with $\mathcal{P}_1$, but temporally separated by an adjustable delay τ_{12}. All experiments have been performed below the static pressure of 0.25 bar, which corresponds to the saturation vapor pressure of acetone at room temperature.

B. Theoretical models

The theoretical results are based on a quantum model and on classical molecular dynamics simulations (CMDSs). In both simulations acetone is treated as an asymmetric-top molecule and the large-amplitude internal rotations of the methyl groups, revealed by the high-resolution investigations of its microwave spectrum, are ignored [31]. The C_{2v} configuration shown in Fig. 1(b) is chosen and the body fixed xyz axis system, coinciding with the principal-axes system, is attached to the molecule using the I^r representation [32]. The twofold axis of symmetry is the $x \, (= b)$ axis and the line joining the two carbon atoms of the methyl groups is parallel to the $z \, (= a)$ axis. After fitting and averaging over tunneling components of the observed microwave and submillimeter wave frequencies [31], the values 0.339424, 0.283865, and 0.163773 cm^{-1} were retrieved for the A, B, and C rotational constants, respectively. Five distortion constants corresponding to Watson's A reduced form [33–35] were also determined and are given in Appendix A. In the body fixed xyz axis system, the 3×3 polarizability tensor $\boldsymbol{\alpha}$ is diagonal with components α_{xx}, α_{yy}, and α_{zz} equal to [36] 46.82, 34.16, and 45.63 a_0^3, respectively.

The first step of the classical calculations consists of the initialization of the center-of-mass positions and translational velocities as well as of the orientations and rotational angular momenta of a large number of acetone molecules. For this, random Euler angles $\theta_m(t = 0)$, $\varphi_m(t = 0)$, and $\psi_m(t = 0)$ are assigned to each molecule m, with the convention that for $\theta_m = \varphi_m = \psi_m = 0$, the body fixed xyz axis system [see Fig. 1(b)] coincides with the space fixed XYZ axis system. Angular speeds $\omega_{m,x}(t = 0)$, $\omega_{m,y}(t = 0)$, and $\omega_{m,z}(t = 0)$ for the rotations around the principal axes of inertia are generated so as to satisfy the Boltzmann equilibrium distribution at 300 K. The needed values of the diagonal components of the inertia tensor $\mathbf{I}$ were obtained from the rotational constants $A = \hbar/(4\pi c I_{zz})$, $B = \hbar/(4\pi c I_{xx})$, and $C = \hbar/(4\pi c I_{yy})$. For the translational motion, random positions of the molecules (but not too close to each other), within a cubic box whose size is defined by the number of molecules and the gas density, and

Boltzmannian velocities were ascribed to the centers of mass in the initialization process. The propagation in time of the orientation, angular speed, position, and translational velocity of all molecules is computed using the equations of classical mechanics, driven by the time dependent force $\mathbf{f}_m(t)$ and torque $\boldsymbol{\tau}_m(t)$ applied to each particle. For the angular variables, the quaternion method is used, based on the definitions and equations given in Sec. 3.3.1 of Ref. [37] and driven by $\boldsymbol{\tau}_m(t)$. For the translation, periodic boundary conditions [37] are used and the centers-of-mass positions are changed according to the translational velocities, the latter being monitored, via the acceleration, by $\mathbf{f}_m(t)$. The values of $\mathbf{f}_m(t)$ and $\boldsymbol{\tau}_m(t)$ resulting from interactions between molecules (collisions) are obtained from the molecules' positions and orientations using the site-site intermolecular potential proposed in Ref. [38]. During the laser pulse(s), the resulting contribution to the torque is computed, in the xyz frame, from $\boldsymbol{\tau}_m(t) = \boldsymbol{\mu}_m(t) \times \mathbf{E}_m(t)$, where the dipole $\boldsymbol{\mu}_m(t)$ induced in the molecule by the laser electric field $\mathbf{E}_m(t)$ is given by $\boldsymbol{\mu}_m(t) = \boldsymbol{\alpha} \cdot \mathbf{E}_m(t)$. In the preceding equations, $\mathbf{E}_m(t)$ is straightforwardly obtained from the laser field in the space fixed axis system, $\mathbf{E}(t) = E_0(t)\mathbf{Z}$, by using $\mathbf{E}_m(t) = \mathbf{A}_m(t)\mathbf{E}(t)$, where $\mathbf{A}_m(t)$ is the rotation matrix associated with the current orientation of the considered molecule. Finally, at each time, the following quantity, which is proportional to the measured birefringence signal [39], is computed,

$$\mathcal{S} \sim \frac{1}{N} \sum_{m=1,N} \sum_{i=x,y,z} \alpha_{ii} \left[\Phi_{Zi}^m(t)^2 - 1/3 \right], \qquad (1)$$

where N is the total number of molecules and $\Phi_{Zi}^m(t)$ denotes the direction cosine between the body-fixed axis i of molecule m and the space-fixed axis Z. For the calculations, the values of the polarizability tensor components given above were used. The laser pulse characteristics were set to those of the experiments.

These CMDSs were used to simulate the measured echo signals but also to provide information on the collisional dissipation of the laser-induced alignment by studying the influence of the gas pressure (as done in Ref. [40] and those cited therein). However, as discussed in Ref. [41], while the CMDSs do enable calculation of the echoes (as shown in Figs. 6 and 8), they do not predict the revivals induced by a single laser pulse, because these are of quantum nature. However, previous studies for a linear [7] and a symmetric-top [42] molecule have shown that the decay time constants of the collisional reduction of the amplitudes of the revivals and echoes are very comparable. We thus carried CMDSs for delays τ_{12} between the two pulses of 13.5 and 9 ps, for which the first- (at $2\tau_{12}$) and second-order (at $3\tau_{12}$) echoes respectively appear near the first revival, shown in Figs. 2 and 4, at 27 ps. The decay time of each of these echoes was then determined from the ratio of their peak-to-dip amplitudes in calculations for the densities of 0.2 and 0 amagat (as done in Ref. [8]). Alternatively, we also computed the echoes for various delays between the laser pulses and analyzed the decay of their amplitudes with τ_{12} at constant gas density (as done in Refs. [7] and [42]). All these exercises lead to consistent results with a decay time constant of 9 ps amagat.
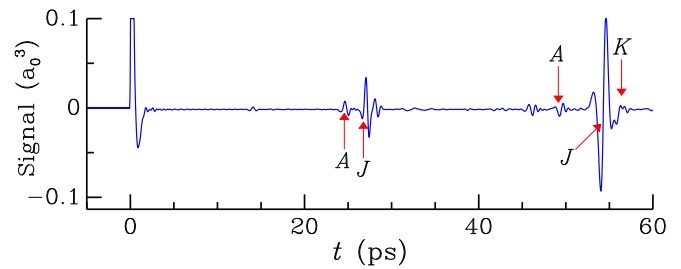

FIG. 2. Time variations of the alignment signal calculated with Eq. (2) for a temperature of 300 K and the same pulse as in Fig. 3. The signal is truncated near $t = 0$. Small arrows are located at the positions of the most prominent revivals identified in Sec. II C.

In the quantum simulations, rotational energies are computed setting up and diagonalizing the matrix of the rotational plus distortion terms Hamiltonian. The basis set functions used are the symmetric-top rotational functions $|J, k, M\rangle$, where J is the total angular momentum, k its projection onto the body fixed z axis, and M its projection onto the space fixed Z axis. The resulting rotational levels are identified with the usual asymmetric-top label JK_aK_c and characterized by Γ their C_{2v} symmetry species. The latter depends on the parity of K_a and K_c; it is A_1, B_1, A_2, and B_2 when K_a, K_c are ee, oe, oo, and eo, respectively. The spin statistical weight of A_1 and A_2 (B_1 and B_2) levels is 28 (36). The coupling of the molecule with the laser field is described by the second-order quadratic Stark coupling Hamiltonian $H_S(t) = -\frac{1}{2}\mathbf{E}(t) \cdot \boldsymbol{\alpha} \cdot \mathbf{E}(t)$, where $\mathbf{E}(t)$ is the laser electric field. The simulation of the signal is based on a calculation similar to that carried out [43] on the H_2S molecule. The reader is referred to that work for the time averaging of the laser electric field, the matrix elements of the Stark coupling Hamiltonian, the form of its matrix, and the time propagation of the rotational wave function. Using the same laser field as for the CMDS approach, we are able to compute the time evolution of the expectation values of the three direction cosines squared, $\langle \Phi_{Zx}^2 \rangle$, $\langle \Phi_{Zy}^2 \rangle$, and $\langle \Phi_{Zz}^2 \rangle$, taking as initial wave function the rotational $|JK_aK_c, M\rangle$ function. From these results, taking a maximum value of J equal to 79 when setting up the Hamiltonian matrix, assuming prior to the pulse a Boltzmannian equilibrium characterized
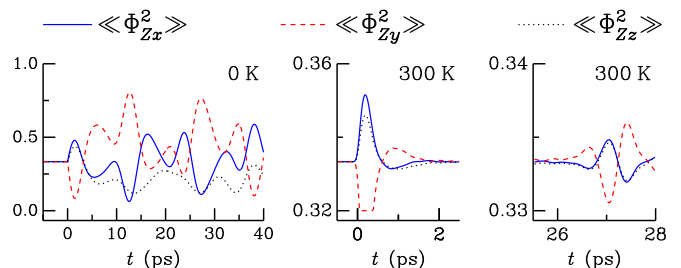

FIG. 3. Time variations of the Boltzmann averaged direction cosines squared when the molecule is subject to a single pulse $\mathcal{P}_1$ with 12 TW/cm^2 intensity at $t = 0$. The left panel shows the variations for a zero temperature; the middle and right panels for a temperature of 300 K. Solid, dashed, and dotted lines correspond to $\langle\!\langle \Phi_{Zx}^2 \rangle\!\rangle$, $\langle\!\langle \Phi_{Zy}^2 \rangle\!\rangle$, and $\langle\!\langle \Phi_{Zz}^2 \rangle\!\rangle$, respectively. For the higher temperature, $\langle\!\langle \Phi_{Zy}^2 \rangle\!\rangle$ is truncated for $0 \leqslant t \leqslant 0.05$ ps.
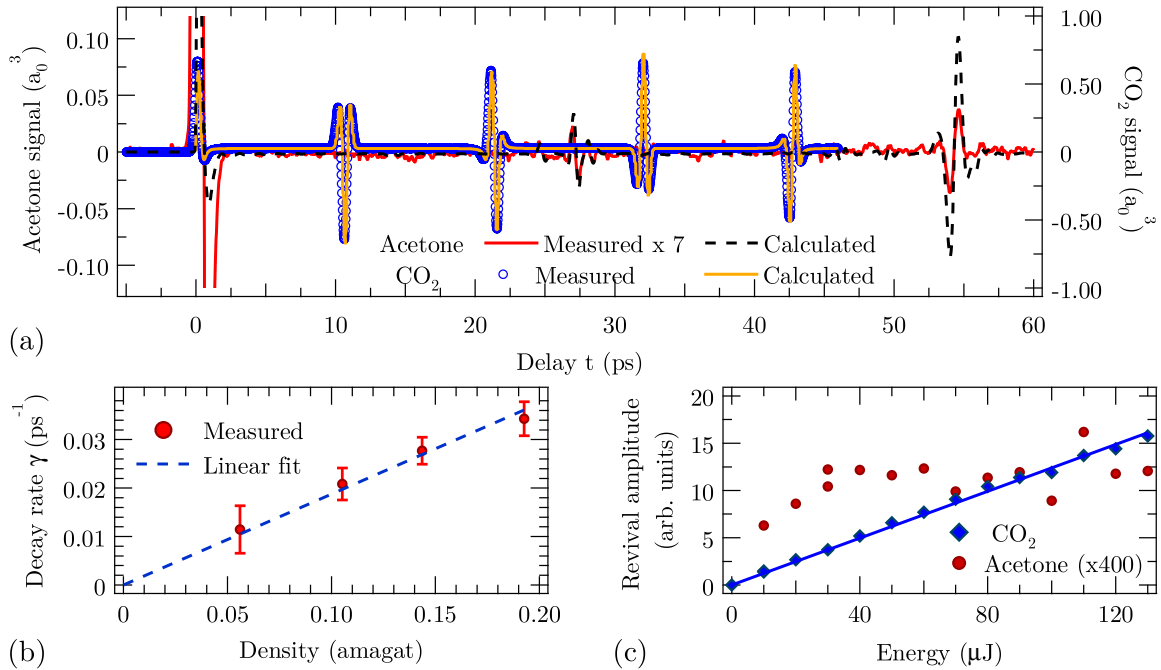
FIG. 4. (a) Alignment signal recorded in 0.15 bar of room-temperature acetone (red solid line) and CO_2 (blue circles) molecules induced by a linearly polarized laser pulse ($\mathcal{P}_1$) of intensity 12 TW/cm^2, and the corresponding quantum simulations for acetone (black dashed line) and CO_2 (yellow solid line) performed in collision-free conditions using Eq. (2). The vertical scales are given in bohr units and the acetone signal is magnified by a factor 7 to help the eyes. (b) Collisional decay rate constant of the alignment revivals of acetone (red solid circles) as a function of the gas density expressed in amagat (1 amagat $\equiv 2.69 \times 10^{25}$ molecules/m^3) with error bars representing one standard deviation. The density normalized decay time constant is obtained from the linear fit applied to the data (blue dashed line). (c) Laser energy dependence of the peak amplitude of the revival of CO_2 (blue diamonds) and acetone (red solid circles) measured under the same experimental conditions (0.15 bar). Linear fit of the CO_2 data (blue solid line).

by a temperature of 300 K, and accounting for the spin statistical weights, we are able to calculate the time dependent thermal averages $\langle\langle \Phi_{Zx}^2 \rangle\rangle$, $\langle\langle \Phi_{Zy}^2 \rangle\rangle$, and $\langle\langle \Phi_{Zz}^2 \rangle\rangle$ as well as the birefringence signal defined in accordance with Eq. (1) as

$$\mathcal{S} \sim \sum_{i=x,y,z} \alpha_{ii} \left(\langle\langle \Phi_{Zi}^2 \rangle\rangle - 1/3 \right). \tag{2}$$

C. Rotational dynamics

In order to understand the rotational dynamics, the effect of a single pulse is investigated theoretically using the quantum approach. Two temperatures are considered: 0 and 300 K. Although the measurements were carried out at room temperature, studying the molecule dynamics at 0 K enables a better grasp of the alignment mechanism.

The short-time dynamics of the molecule when subject to a single pulse can be understood with the help of Fig. 3 showing the time variations of the direction cosines squared computed for temperatures of 0 and 300 K. As expected, a much slower dynamics is observed for the lower temperature than for the higher, since the frequency beating between the rotational transitions at 0 K involves a small number of states. In both cases, an antialignment of the body fixed y axis and nearly identical alignment of the x and z axes take place within 2 ps from the pulse. This stems from the y axis being the least polarizable axis while the more polarizable x and z axes are characterized by nearly identical polarizability. The behavior

of the molecule is quite different from that of ethylene where the a axis is far more polarizable than the b and c axes [44]. This is confirmed by a unitless tensorial components ratio $\alpha_0^2/\alpha_2^2 = \sqrt{2/3}(2\alpha_{zz} - \alpha_{xx} - \alpha_{yy})/(\alpha_{xx} - \alpha_{yy})$ [43,45] as large as 5.89 for ethylene and as small as 0.66 for acetone. For the lower temperature, between 5 and 40 ps after the pulse, the ensuing dynamics is dominated by opposite phase revivals in $\langle\langle \Phi_{Zx}^2 \rangle\rangle$ and $\langle\langle \Phi_{Zy}^2 \rangle\rangle$ describing a rotation of the molecule around its z axis, which is a stable axis of rotation in the classical limit. This is consistent with the smallness of the ratio α_0^2/α_2^2 since α_0^2 may be considered as being responsible for a single axis alignment and α_2^2 for a rotation of the body around this single axis [46]. A value of $\langle\langle \Phi_{Zz}^2 \rangle\rangle$ smaller than 1/3 and somewhat constant can be interpreted as the z axis remaining delocalized in the XY plane. For the higher temperature, between 2 and 40 ps after the pulse, the three direction cosines display almost no variations except near 25 and 27 ps, where the A- and J-type revivals, respectively, take place. These are described in the next paragraph. Near this region, from 26 to 28 ps, the variations depicted in Fig. 3 show a behavior that mimics the one after the pulse. An antialignment (followed by an alignment) of the body fixed y axis and nearly identical alignment (followed by antialignment) of the x and z axes can be observed, with a much reduced planar delocalization of the z axis as compared to 0 K.

The birefringence signal calculated at 300 K is shown in Fig. 2. The position of the depicted alignment revivals can be

calculated starting from the rotational wave packet after the pulse. As it evolves under the field-free Hamiltonian, it can be written

$$|\Psi_M\rangle = \sum_{JK_aK_c} c_{JK_aK_c}^M e^{-i2\pi c E_{JK_aK_c}t}|JK_aK_c, M\rangle, \qquad (3)$$

where $E_{JK_aK_c}$ is the field-free rotational energy in cm^{-1}, c is the speed of light in cm s^{-1}, and $c_{JK_aK_c}^M$ is an expansion coefficient depending on the initial wave function and the interaction with the pulse. As the Stark coupling Hamiltonian belongs to the A_1 symmetry species of C_{2v}, the rotational levels in Eq. (3) belong to the same symmetry species. The contribution from the rotational wave packet in Eq. (3) to the transient birefringence signal is written

$$S'(t) = \sum_{n \neq n'} F_{n,n'}^M \exp[-i2\pi c(E_{n'} - E_n)t] + \text{c.c.}, \qquad (4)$$

where the static term, i.e., the permanent alignment component, has been disregarded. In this expression, n and n' are shorthand notations for the rotational quantum numbers and the complex amplitude $F_{n,n'}^M$ takes the form

$$F_{n,n'}^M = \rho_{nn'}^M \langle n| \sum_{i=x,y,z} \alpha_{ii} \Phi_{Zi}^2 |n'\rangle, \qquad (5)$$

with $\rho_{nn'}^M$ denoting the coherence between $|n\rangle$ and $|n'\rangle$ states of same M value. This equation emphasizes that the complex amplitude mainly depends on the matrix element of the birefringence signal operator in Eq. (2). This matrix element is nonvanishing provided the selection rules $K_a - K_a' = 0, \pm 2$; $K_c - K_c' = 0, \pm 2$; and $|J - J'| \leqslant 2$ are fulfilled. As in Refs. [13,47], these selection rules and the expression of the rotational energy in the high K_a or K_c limit allow us to retrieve the rotational coherences giving rise to revivals. In the high-K_c limit, J-type features $\Delta K_c = 0$ ($K_c \approx J$) with $\Delta J = 1$ and 2 coherences associated with energy differences $\Delta E = (A + B)(J + 1)$ and $(A + B)(2J + 3)$, respectively, are found. They are produced at $t = p/[2c(A + B)] = pT_J$ (with $T_J = 26.740$ ps), where $p \geqslant 1$ is an integer. K-type $\Delta J = 0$ and $\Delta K_c = \pm 2$ ($K_c \approx J$) coherences lead to transients at $t = p/[c(2A + 2B - 4C)] = pT_K$ (with $T_K = 56.355$ ps). A-type $\Delta J = \Delta K_a = \pm 2$ lead to transients at $t = p/(4cA) = pT_A$ (with $T_A = 24.551$ ps) in the high-K_a limit. Finally, C-type $\Delta J = \Delta K_c = \pm 2$ lead to transients at $t = p/(4cC) = pT_C$ (with $T_C = 50.883$ ps) in the high-K_c limit. The associated transients (J, K, and A type) which could be found in the calculated birefringence signal of Fig. 2 are indicated in this figure. Although in this figure the strength of the J-type transients seems to increase with time, these transients actually display an alternating magnitude [44,48] leading to a third transient weaker than the second. The reason is that $\Delta J = \pm 1$ transitions produce J-type transients with a period that is twice compared to $\Delta J = \pm 2$ transitions. A numerical calculation carried out up to $t = 250$ ps confirms that the third J-type revival is indeed weaker that the second. This calculation also demonstrates that the revival strengths decrease with time mainly because of the molecule asymmetry, with a small influence of centrifugal distortion.

D. Experimental results and discussion

1. Rotational revivals

First, we start with a standard alignment scheme using a single pump-pulse excitation ($\mathcal{P}_1$). Figure 4(a) presents a comparison between recorded alignment signal and result of the collision-free quantum simulations for acetone gas (left vertical scale). The first and second revivals predicted in Sec. II C near 27 and 54 ps can be seen, but with a very small amplitude. The weakness of the signal is due to several reasons. First, as mentioned in the introduction, asymmetric-top molecules are more difficult to align if one compares to symmetric-top and linear molecules exhibiting much more regular rotational features. Second, the collisional decay time constant of acetone is short due to the strong and long-range dipole-dipole interaction involved in collisions between acetone molecules (see discussion below), reducing therefore the amplitude of the revivals that occur at relatively long time delays. This signal damping due to collisions is evidenced by comparing in Fig 4(a) the relative amplitudes of the first and second revival J-type transients in both the experiment and the simulation performed in collision-free conditions.

To corroborate both statements, we performed additional measurements. First, we measured the ratio R of the second to the first revival amplitudes and compared this number to the value computed with the help of Eq. (2), so as to evaluate the decay rate constant of gas acetone defined as

$$\gamma = -\frac{1}{\tau_J} \ln\left(\frac{R_{\text{exp.}}}{R_{\text{th.}}}\right), \qquad (6)$$

with τ_J the time interval between the first and second revivals of the J-type transient. As shown in Fig. 4(b), in order to assess the consistency of our measurements, we repeated this exercise for different gas densities d and then fitted the linear dependence $\gamma = \gamma_0 d$ in order to extract the density normalized collisional decay time constant $t_c = \gamma_0^{-1} = 5.4 \pm 0.4$ ps amagat of the acetone vapor. This value is in reasonable agreement with the CMDS prediction of 9 ps amagat obtained in Sec. II B with a simple acetone-acetone potential. These decay time constants for pure acetone are significantly smaller than those obtained from measurements and requantized CMDSs of revival decay time constants in the cases of pure ethane (~ 48 ps amagat [29,40]) and pure carbon dioxide (~ 65 ps amagat [49,50]). Besides mass effects, this is mainly due to the fact that acetone-acetone collisions involve much longer-range and stronger anisotropic forces than do those between C_2H_6 (and CO_2) pairs. This results from the strong electric dipole of acetone (~ 2.90 debye [51,52]), leading to large interaction energies in R^{-3} (with R the intermolecular distance), and the fact that the two other molecules only possess a quadrupole moment inducing a weaker and shorter range (in R^{-5}) intermolecular potential.

Next, in order to compare the alignment efficiency of acetone with reference to a known system, we performed measurements and calculations substituting the acetone with CO_2 and keeping the same experimental conditions. As shown in the right vertical scale of Fig. 4(a), the amplitudes of the revivals as well as that of the permanent alignment
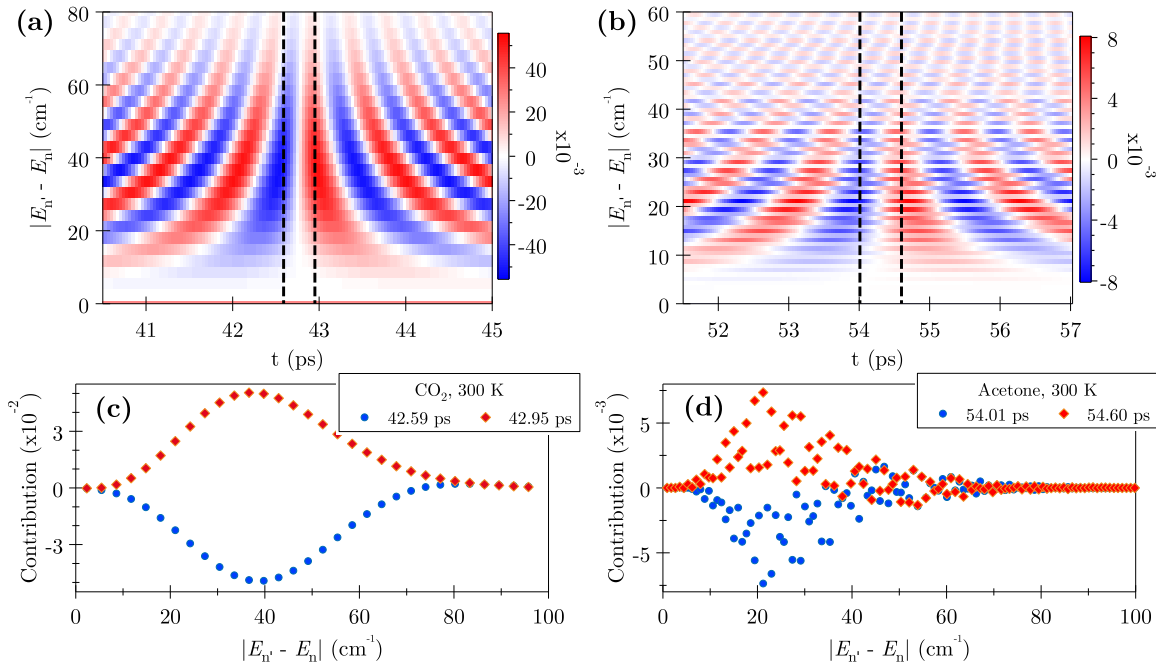
FIG. 5. Summed up contributions of the coherences of same $|E_{n'} - E_n|$ value to the alignment signals [see Eq. (4)] as a function of $|E_{n'} - E_n|$ and time t, for CO_2 [(a), (c)] around the 4th revival and acetone around the 2nd revival [(b), (d)]. The vertical dashed lines in the color maps [(a), (b)] indicate the positions of the minimum and maximum alignments [see Fig. 4(a)] on both sides of the considered revival. The plots (c) and (d) display the values at these specific times. Note that the sum of all values along any vertical line (i.e., for a given time t) in (a) or (b) gives the value, for the corresponding time t, displayed in Fig. 4(a).

(recognizable by the asymmetrical shape of the transients [53]; see, e.g., the third revival) of CO_2 are very well reproduced by the quantum model. The transient and permanent components being respectively proportional to I_1 and I_1^2 [53,54], this confirms the estimated intensity I_1 of P_1. Because the collisional decay of the alignment signal of CO_2 is negligible [49] at the considered pressure under the present temporal range, the amplitudes of the CO_2 and acetone experimental signals depicted in Fig. 4(a) are scaled by matching the CO_2 signal to the theory.

Although the difference between the largest and smallest polarizability components is comparable for the two molecules, the collision-free calculations predict an amplitude of the second revival of acetone about 7 times weaker than the third revival of CO_2. This can be explained by the fact that for asymmetric-top molecules, only a small part of the laser pulse is transferred to the subsets of rotational transitions leading to a rephasing of the rotational wave packet at specific times. This was shown in Sec. II C in the limiting case of high K_a or K_c values, where only some specific transitions contribute to a given revival (e.g., J type). No such limit holds for linear molecules, while for symmetric-top molecules, the energy transferred to the subsets by the same laser pulse is larger if one assumes that both molecules exhibit the same anisotropy of polarizability between the largest and smallest components. These statements are confirmed by the results in Fig. 5, where for each discrete energy separation $|E_{n'} - E_n|$ defined in Eq. (4), the corresponding complex amplitude $F_{n,n'}^M$ factors of Eq. (5) are summed up and displayed at different times of the system evolution. Indeed, one clearly sees that while all significantly populated coherences contribute with

consistent magnitudes to the alignment minimum (at 42.59 ps) and maximum (at 42.95 ps) on both sides of the 4th revival of CO_2, it is not the case for the 2nd J-type revival of acetone to which coherences somehow *inconsistently* contribute to the minimum (at 54.01 ps) and maximum (at 54.60 ps) alignment. Furthermore, the magnitudes of the contributions to the alignment (see scales) are much smaller in the case of acetone than they are for CO_2. These two facts explain the large difference between the magnitudes of the computed alignments of CO_2 and acetone shown in Fig. 4(a). However, the experimental ratio of the CO_2 third revival to the acetone second J-type revival is found to be 121, which is much larger than the value of 7 found with the collision-free calculation of Sec. II C and of 29 predicted by the quantum simulations when the measured value of γ_0 is included in the calculation. We believe that this important discrepancy results from the photodissociation of the acetone molecule induced by the strong pump pulse, which is the third reason for the weakness of the revivals. This statement is supported by the energy dependence of the alignment signals observed for both molecules. Indeed, Fig. 4(c) shows the amplitude of the alignment signal versus the energy of the pump pulse recorded in CO_2 (third revival) and acetone (second revival) under the same experimental conditions. In the present intensity regime, the simulations for both molecules predict a revival amplitude scaling linearly with the pump intensity. While this is experimentally confirmed for CO_2, the alignment signal recorded in acetone exhibits a clear saturation effect. It is known that the single-photon excitation of the S_1 exited state of acetone at a wavelength close to 266 nm leads [55–58] to an efficient C-C bond breakage (with a quantum yield reaching

1 at 256.4 nm). We believe that the resonant excitation of the S_1 state also takes place via a three-photon process driven by the pump pulse at 800 nm, probably with a different rate than for a single-photon excitation but with enough efficiency to deplete the number of acetone molecules in the interaction region and hence to reduce the alignment signal. The amount of molecules possibly lost through excitation of the S_1 state can be estimated from the energy dependence of the alignment signal depicted in Fig. 4(c). This plot shows that the departure of the signal from the linear dependence is already achieved at the lowest investigated energy of 10 μJ. If we assume that below this value the linearity of the signal would be satisfied if we were able to detect it, by drawing a line joining the origin of the graph to the signal measured at 10 μJ, and extrapolating it up to the abscissa of 35 μJ corresponding to the intensity of 12 TW/cm^2 used in the results of Fig. 4(a), we can estimate that at least 50% of the molecules have not been aligned by the pulse. This is a lower limit, since we do not know from which energy value the saturation sets in. In addition, as discussed above, the quantum simulations predict an acetone signal that is $121/29 \approx 4$ times larger than what is observed. Based on the above, we can reasonably estimate that between 50% and 75% of the ground state population is promoted to the excited state. The competition between the dissociation of the parent molecule and its alignment by the pump pulse can explain the saturation of the signal observed in Fig. 4(c) and therefore the unexpected weakness of the acetone signal observed in Fig. 4(a).

2. Rotational echoes

In order to enhance the alignment of acetone under field-free conditions, we generated rotational echoes by introducing a second pump pulse $\mathcal{P}_2$ at time τ_{12} after $\mathcal{P}_1$. It should be stressed that rotational echoes are to be distinguished from optimization of one-dimensional [59,60] or three-dimensional [46] field-free alignment of molecules by multiple-pulse laser excitation. In the latter, enhanced alignment occurs at or close to a revival, whereas in the former the echo occurs outside a revival's area. The results of Fig. 6(a) have been obtained by setting τ_{12} to 4.93 and 6.11 ps, respectively, keeping the pressure and intensity of $\mathcal{P}_1$ identical to the previous measurements. Four alignment echoes are observed, the first- and the second-order echo produced at times τ_{12} and $2\tau_{12}$ after $\mathcal{P}_2$, respectively, and small fractional echoes produced at $\frac{1}{2}\tau_{12}$ and $\frac{3}{2}\tau_{12}$, their existence being well predicted by both theoretical models depicted in Fig. 6(b). The vertical scales of Figs. 4(a) and 6(a) are identical, allowing a direct signal comparison between the single- and double-pump experiment. As shown, the echo-assisted alignment signal is twice the amplitude of the largest revival observed in the standard alignment trace reported in Fig. 4(a). The first- and the second-order echoes, as well as others of higher order at $3\tau_{12}$, $4\tau_{12}$, etc., are the only ones observed in linear molecules with detections sensitive to $\langle \cos^2(\theta) \rangle$ [8,30,61]. The fractional echoes have only been observed in linear molecules optically probed through third- [62] or higher-order harmonic generation [63] sensitive to higher-order observables ($\langle \cos^{2n}(\theta) \rangle$, $n > 1$) or by means of the cold target recoil ion momentum spectroscopy technique [64]. In order to explain the presence
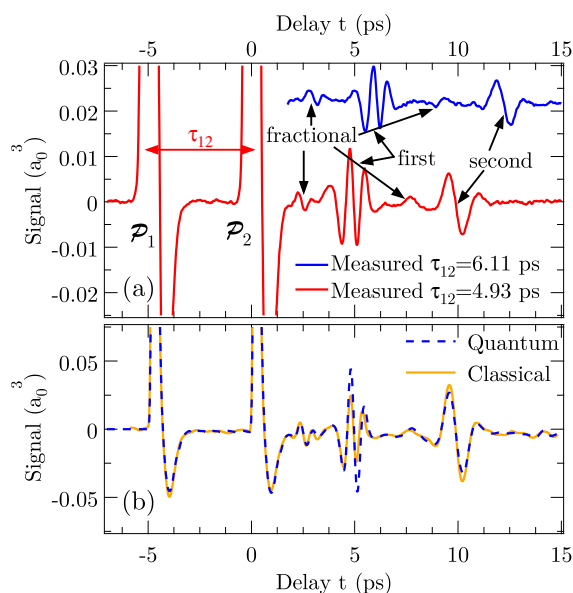

FIG. 6. (a) Alignment echoes measured in acetone stimulated by two pump pulses $\mathcal{P}_1$ (12 TW/cm^2) and $\mathcal{P}_2$ (12 TW/cm^2) with delays of $\tau_{12} = 4.93$ (red solid line) and 6.11 ps (upshifted, blue solid line), respectively, for a pressure of 0.15 bar. Same conditions as in Fig. 4(a). The first- and second-order echo, as well as the fractional echoes, are indicated by arrows. (b) Quantum (blue dashed line) and classical (yellow solid line) simulated signal calculated from Eqs. (1) and (2), respectively, for $\tau_{12} = 4.93$ ps.

of these fractional echoes in the measure of $\langle \cos^2(\theta) \rangle$ for acetone, let us recall that echo phenomena, such as spin [65] and photon [66] echoes, are usually interpreted in quantum mechanics using the time-reversal argument. The phase accumulated by the system between the two pulses and the one acquired by the system from the second pulse until the time of observation of the echo compensate each other. In other words, the second pulse formally reverses the course of time, bringing back the system to its starting point. The same arguments apply to rotational echoes. However, the interpretation is a little more complex [61] since molecular alignment occurs in a multilevel system. As for photon or spin echoes, rotational echoes arise through a nonlinear process involving constructive interference between quantum pathways [41,67]. In an asymmetric-top molecule, one of them can be clearly identified as responsible for the presence of a fractional echo in the birefringence signal. Figure 7 displays its corresponding Feynman diagram. Starting from an asymmetric-top energy level characterized by J and a high K_c value so that an asymptotic expression of the rotational energy can be used, $\mathcal{P}_1$ gives rise to a J-type $\Delta J = 1$ and $\Delta K_c = 0$ coherence associated with the frequency $\omega_{J+1,J} = 2\pi c(A+B)(J+1)$. As emphasized by Eq. (4), its accumulated phase is $\varphi_1 = \omega_{J+1,J} \tau_{12}$ at the time of $\mathcal{P}_2$. Via two successive impulsive Raman transitions, marked $\mathcal{P}_2^{(1)}$ and $\mathcal{P}_2^{(2)}$ in Fig. 7, this second pulse creates a J-type $\Delta J = 2$ and $\Delta K_c = 0$ coherence associated with the frequency $\omega_{J,J+2} = -2\pi c(A+B)(2J+3)$ and to an accumulated phase $\varphi_2 = \omega_{J,J+2}T$ at time T after $\mathcal{P}_2$. In the high-J limit, these phases compensate each other provided that $\varphi_1 + \varphi_2 = 0$ yielding a
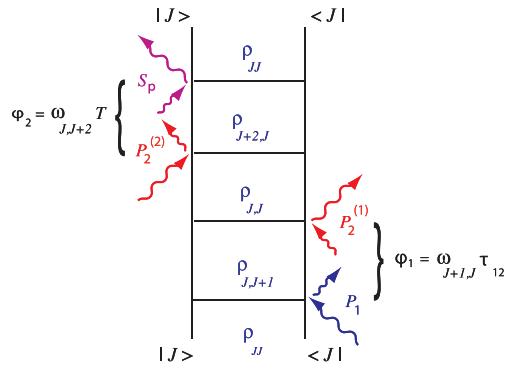
FIG. 7. Double-sided Feynman diagram corresponding to one of the quantum pathways leading to a fractional echo. A pair of wavy arrows illustrates an impulsive Raman transition leading to an increase (long followed by a short arrow) or a decrease (short followed by a long arrow) of the rotational energy of the system (see, e.g., Ref. [61]) as a result of its interaction with $\mathcal{P}_1$, $\mathcal{P}_2$, and the probe pulse $\mathcal{S}_p$ (signal).

rephasing of the system, i.e., a fractional echo, at $T \approx \frac{1}{2}\tau_{12}$. Note that the two above-mentioned coherences rephase regardless of J and of the associated rotational constant. This implies that, as for the full echo in linear molecules [41], the fractional echo is here also a classical phenomenon. This explains why it is predicted by the purely classical approach [see Fig. 6(b)].

In the case of a symmetric-top molecule, the preceding results still hold because these molecules also display J-type $\Delta K = 0$ coherences with $\Delta J = \pm 1$ and ± 2. The fact that the observation of fractional echoes was not reported by previous studies of such species [42,61] must be ascribed to the weakness of the effect. In the case of a linear molecule, fractional echoes are not observed [8,30,61] because $\Delta J = \pm 1$ coherences do not arise.

The above arguments demonstrate that the observation of a fractional echo in the present work is related to the nonlinearity of the molecule, which in itself constitutes an important outcome of this work. Alignment echoes can potentially reveal the nonlinear nature of an unknown system.

III. THIRD-HARMONIC GENERATION IN ALIGNED ACETONE MOLECULES

Since a field-free aligned sample of room-temperature acetone can be produced using the echo technique, it can be potentially used for applications requiring an anisotropy of the molecules' orientations. As a proof of principle, we have investigated a nonlinear coherent process that necessarily requires a prealigned sample of molecules. It is known that a circularly polarized (CP) light cannot drive a nonlinear optical conversion process in a centrosymmetric medium [68], which explains that harmonic radiations generated by CP light cannot take place in a gas of atoms or of randomly oriented molecules. However, it has been demonstrated that third-harmonic generation (THG) [62,69], as well as higher-order harmonic generation [70], occurs in a sample of prealigned molecules, thanks to the axial symmetry breaking of the
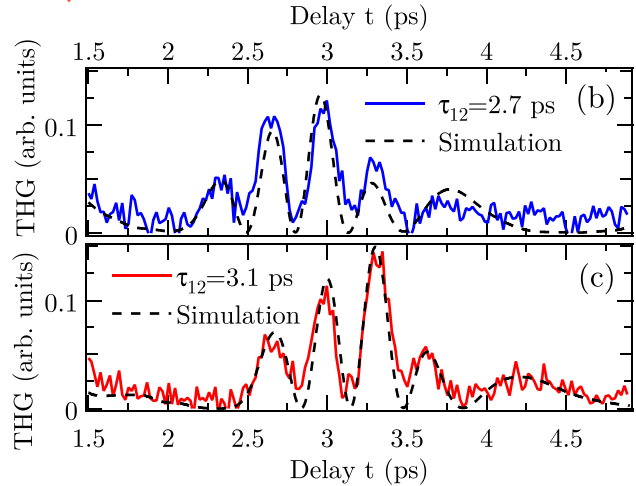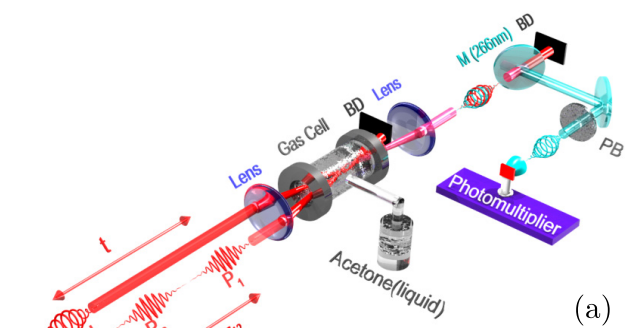

FIG. 8. (a) Third-harmonic generation setup. BD: beam dump, PB: passband filter (250–280 nm). Echoes observed in the third-harmonic signal generated by a circularly polarized fundamental pulse (Fund.) in acetone molecules (solid lines) aligned by two pump pulses $\mathcal{P}_1$ and $\mathcal{P}_2$ temporally delayed by $\tau_{12} = 2.7$ (b) and 3.1 ps (c) at 0.1 bar, respectively, with the corresponding numerical classical simulations (dashed lines). The quantum results (not shown) are indistinguishable from the classical ones for the scale of the present figure.

molecule+field system. Hereafter, the alignment echo of acetone was used to generate the third harmonic of a CP radiation using the setup described in Fig. 8(a). In contrast to the previous experiment, the wavelength of the third beam was set to 800 nm, its input polarization was circular, and the THG radiation of the fundamental radiation was detected by a photomultiplier tube (blind at 800 nm), combining dichroic mirrors and a bandpass filter in order to remove the residual 800 nm radiation. The alignment echo-assisted THG signals obtained for two different delays τ_{12} are depicted in Figs. 8(b) and 8(c). It is important to mention that no THG could be detected when the molecules were field-free aligned with a single-pump pulse. This results from the collisional dissipation for the THG signal, proportional to the intensity of the THG field, being twice faster than for the birefringence signal measured with a balanced detection, proportional to the field amplitude. As shown by Figs. 8(b) and 8(c), the rotational echo enables us to overcome this limitation by substantially aligning the molecules before the revivals. The THG signal produced from aligned molecules can be used to assess the second-order electric hyperpolarizabilities $\boldsymbol{\gamma}$ of the molecule.

Figure 8 also presents the calculated THG intensities, defined as $I_3(t) \approx \widetilde{\mathbf{E}}_3(t)\widetilde{\mathbf{E}}_3^*(t)$, with $\widetilde{\mathbf{E}}_3(t) = \widetilde{E}_{3_Y}(t)\mathbf{Y} + \widetilde{E}_{3_Z}(t)\mathbf{Z}$ the

third-harmonic field, computed from the following expressions:

$$\widetilde{E}_{3_Y}(t) \approx \frac{3}{4}\widetilde{E}_1^3(t)\left\{a_x\left(\langle\!\langle\Phi_{Zx}^4\rangle\!\rangle - \frac{1}{5}\right) + b_{Yx}\left(\langle\!\langle\Phi_{Zx}^2\rangle\!\rangle - \frac{1}{3}\right) + a_z\left(\langle\!\langle\Phi_{Zz}^4\rangle\!\rangle - \frac{1}{5}\right) + b_{Yz}\left(\langle\!\langle\Phi_{Zz}^2\rangle\!\rangle - \frac{1}{3}\right) + c_{xz}\left(\langle\!\langle\Phi_{Zx}^2\Phi_{Zz}^2\rangle\!\rangle - \frac{1}{15}\right)\right\},$$

(7)

$$\widetilde{E}_{3_Z}(t) \approx -i\widetilde{E}_1^3(t)\left\{a_x\left(\langle\!\langle\Phi_{Zx}^4\rangle\!\rangle - \frac{1}{5}\right) + b_{Zx}\left(\langle\!\langle\Phi_{Zx}^2\rangle\!\rangle - \frac{1}{3}\right) + a_z\left(\langle\!\langle\Phi_{Zz}^4\rangle\!\rangle - \frac{1}{5}\right) + b_{Zz}\left(\langle\!\langle\Phi_{Zz}^2\rangle\!\rangle - \frac{1}{3}\right) + c_{xz}\left(\langle\!\langle\Phi_{Zx}^2\Phi_{Zz}^2\rangle\!\rangle - \frac{1}{15}\right)\right\},$$

(8)

assuming a fundamental field defined as $\widetilde{\mathbf{E}}_1(t) = \frac{1}{\sqrt{2}}\widetilde{E}_1(t)(\mathbf{Y} + i\mathbf{z})$. The coefficients a_x, a_z, b_{Yx}, b_{Yz}, b_{Zx}, b_{Zz}, and c_{xz} are defined as functions of the electric hyperpolarizabilities γ_{ij} of the molecule (see Appendix B). As previously mentioned, for randomly aligned molecules, where $\langle\Phi_{Ij}^4\rangle = \frac{1}{5}$, $\langle\Phi_{Ij}^2\rangle = \frac{1}{3}$, and $\langle\Phi_{Ii}^2\Phi_{Ij}^2\rangle = \frac{1}{15}$ for $i \neq j$, no harmonic field is produced. Details about the derivation of Eqs. (7) and (8) and determination of the hyperpolarizabilities of acetone are provided in Appendices B and C, respectively. According to the simulations, the echo-assisted THG signal is dominated by the three observables $\langle\Phi_{Zz}^4\rangle$, $\langle\Phi_{Zz}^2\rangle$, and $\langle\Phi_{Zx}^2\Phi_{Zz}^2\rangle$ weighted, respectively, by the coefficients a_z, b_{Yz} and b_{Zz}, which combine the six independent elements of the hyperpolarizability. The good match between the calculated and observed THG echoes allows a validation of the relative values of the calculated hyperpolarizability components given in Table I (basis A, MP2). A thorough assessment of the latter values could be achieved by analyzing the THG field components [69] as a function of polarization of the aligning and fundamental pulses.

TABLE I. Electric (hyper)polarizability for acetone at the theoretical MP2(FULL)/cc-pvdz geometry (all properties in atomic units).

Property	Basis A		Basis B	
	SCF	MP2	SCF	MP2
μ_x	−1.3659	−1.1540	−1.3637	−1.1510
α_{xx}	44.4831	47.0722	44.4958	47.0972
α_{yy}	32.9569	34.3373	33.0184	34.0361
α_{zz}	42.0303	45.9333	42.0876	46.0413
$\overline{\alpha}$	39.8235	42.4476	39.8673	42.5249
$\Delta\alpha$	−7.37	1.48	−8.35	0.86
β_{xzz}	10.5165	12.2053	10.4828	12.1676
β_{xyy}	28.01	27.60	27.17	24.58
β_{xxx}	56.81	22.91	58.93	25.86
$\overline{\beta}$	46.47	31.19	46.66	30.78
γ_{xxxx}	3884	6232	4203	6973
γ_{yyyy}	2854	3820	2963	4024
γ_{zzzz}	7389	13811	7548	14176
γ_{zzyy}	1246	2085	1296	2243
γ_{yyxx}	1281	1856	1375	2042
γ_{xxzz}	2327	4510	7463	4835
$\overline{\gamma}$	4767	8153	4996	8683

IV. CONCLUSION

We have shown that field-free alignment of the acetone molecule is hardly achievable at room temperature. The first reason is that acetone has a very small asymmetry parameter, much closer to zero than any other molecules that have been so far aligned by laser pulses. The incommensurability of its rotational spectrum, which translates, in the temporal domain, to a poor periodicity of the rotational motion at room temperature, results in the production of quick and fast vanishing weak alignment revivals. The second explanation is that gas-phase acetone is exposed to a fast collisional dissipation resulting from a large dipole-dipole interaction between molecules. This is revealed by our analysis performed at different gas densities, which leads to a measured collisional decay time constant of 5.4 ± 0.4 ps amagat. Finally, the alignment of acetone at 800 nm seems to be strongly reduced by a concomitant near-resonant multiphoton dissociation process of the molecule. In order to improve the alignment efficiency, rotational echoes were generated by submitting the molecules to a sequence of two short laser pulses. In this way, a rotational alignment echo with twice the amplitude of the largest revival could be observed, along with second-order and fractional echoes, using a birefringence detection. It is the first time that the latter type of echo is observed in an asymmetric-top molecule. We show that these fractional echoes are attributed to the nonlinear structure of the molecule, which provides us with a tool to evaluate its linear or nonlinear nature without prior detailed analysis. Our findings are fully supported by classical molecular dynamics simulations and quantum calculations. Finally, as an illustration of possible applications, rotational echoes of aligned acetone were used to generate the third-harmonic radiation from a circularly polarized fundamental field. Echoes are particularly relevant in this case, since no harmonic radiation could be detected when acetone was aligned by using a single-pulse excitation. Furthermore, our study enables us to test the values of the second-order hyperpolarizability tensor calculated in this work. Indeed, the simulation of the alignment-echo-assisted harmonic signal requires the knowledge of both the electric polarizability and second-order hyperpolarizability. Only the first tensor was so far known from literature. The second one was hence determined using a finite-field perturbation theory and coupled cluster calculations. A comparison between the recorded signals and the quantum and classical simulations of the harmonic signal validated the successful test of the six

independent components of the hyperpolarizability tensor of acetone.

APPENDIX A: DISTORTION CONSTANTS

Rotational distortion effects are accounted for using a Watson type [71] effective rotational Hamiltonian H_R. It is expressed as follows in terms of the rotational constants and the quartic first-order distortion parameters,

$$
\begin{aligned}
H_R = {} & A J_z^2 + B J_y^2 + C J_z^2 - \Delta_K J_z^4 \\
& - \Delta_{KJ} \mathbf{J}^2 N_z^2 - \Delta_J \mathbf{J}^4 - \left[\delta_K J_z^2 + \delta_J \mathbf{J}^2, J_{xy}^2 \right]_+, \quad \text{(A1)}
\end{aligned}
$$

where J_x, J_y, and J_z are body fixed components of the rotational angular momentum; $J_{xy}^2 = J_x^2 - J_y^2$; $[,]_+$ is the anticommutator; A, B, and C are the rotational constants; and Δ_K, Δ_{KJ}, Δ_J, δ_K, and δ_J are the quartic first-order distortion parameters. The values used in this work are -0.770064, 1.216119, -0.0179238, 0.265816, and -0.017583×10^{-6} cm^{-1}, respectively.

APPENDIX B: THIRD-HARMONIC GENERATION IN ALIGNED ASYMMETRIC-TOP MOLECULES

Working in the framework of perturbation theory and neglecting dispersion, the third-harmonic field $\mathbf{E}_3(t)$ produced at frequency $\omega_3 \approx 3\omega_1$ can be estimated from the constitutive relations relating the macroscopic nonlinear polarization $\mathbf{P}^{(3)}(t)$ to the electric field $\mathbf{E}_1(t)$ at the fundamental frequency ω_1

$$
\mathbf{P}^{(3)}(t) = \varepsilon_0 \chi^{(3)} \vdots \mathbf{E}_1(t) \mathbf{E}_1(t) \mathbf{E}_1(t), \quad \text{(B1)}
$$

where ε_0 is the vacuum permittivity and $\chi^{(3)} = \chi^{(3)}(-\omega_3; \omega, \omega, \omega)$ is the third-order nonlinear susceptibility tensor of the medium. Using Kleinman's symmetry relation and considering that the fundamental field propagating along $\mathbf{X}$ is circularly polarized, $\widetilde{\mathbf{E}}_1(t) = \frac{1}{\sqrt{2}} \widetilde{E}_1(t)(\mathbf{Y} + i\mathbf{Z})$, with $\widetilde{E}_1(t)$ the complex amplitude of $E_1(t)$, the *body fixed* components of the THG field are given by the following expressions:

$$
\widetilde{E}_{3_Y}(t) \approx \widetilde{E}_1^3(t) \left(\chi_{YYYY}^{(3)} - 3\chi_{YYZZ}^{(3)} \right), \quad \text{(B2)}
$$

$$
\widetilde{E}_{3_Z}(t) \approx \widetilde{E}_1^3(t) \left(-i\chi_{ZZZZ}^{(3)} + 3i\chi_{ZZYY}^{(3)} \right). \quad \text{(B3)}
$$

The matrix elements of the tensor $\chi^{(3)}$ can be derived from the components of the second-order hyperpolarizability tensor γ using the rotation matrix involving the three Euler angles θ,

φ, and χ:

$$
\chi_{IJKL}^{(3)} = N_0 \Phi_{Ii} \Phi_{Jj} \Phi_{Kk} \Phi_{Ll} \gamma_{ijkl}, \quad \text{(B4)}
$$

where N_0 is the number density and where Φ_{Ii} defines the direction cosines of the angle between the molecule fixed frame ($i = x, y, z$) axis and the space fixed frame ($I = X, Y, Z$) axis [72]. Here summation over the repeating indices is assumed. For an asymmetric-top molecule, the 81 nonvanishing components of the hyperpolarizability can be expressed in terms of six independent elements, $\gamma_{xxxx} = \gamma_{xx}$, $\gamma_{yyyy} = \gamma_{yy}$, $\gamma_{zzzz} = \gamma_{zz}$, $\gamma_{xxyy} = \gamma_{xy}$, $\gamma_{xxzz} = \gamma_{xz}$, and $\gamma_{yyzz} = \gamma_{yz}$, whose calculation is described in Appendix C. Using Eqs. (B2)–(B4), and considering that the aligning field is linearly polarized along the Z axis and therefore leaves the rotation φ invariant around the Z axis, the THG field components $\widetilde{E}_{3_Y}(t)$ and $\widetilde{E}_{3_Z}(t)$ can be calculated for any orientation of the molecule defined by the two Euler angles θ and χ using, respectively, Eqs. (7) and (8) of the main text, with coefficients defined as

$$
\begin{aligned}
a_x &= 5(\gamma_{xx} - 6\gamma_{xy} + \gamma_{yy}), \\
a_z &= 5(\gamma_{yy} - 6\gamma_{zy} + \gamma_{zz}), \\
b_{Yx} &= 2(-3\gamma_{xx} + 15\gamma_{xy} - 2\gamma_{yy} - 3\gamma_{zx} + 3\gamma_{zy}), \\
b_{Yz} &= 2(3\gamma_{xy} - 2\gamma_{yy} - 3\gamma_{zx} + 15\gamma_{zy} - 3\gamma_{zz}), \\
b_{Zx} &= (-3\gamma_{xx} + 30\gamma_{xy} - 7\gamma_{yy} - 3\gamma_{zx} + 3\gamma_{zy}), \\
b_{Zz} &= (3\gamma_{xy} - 7\gamma_{yy} - 3\gamma_{zx} + 30\gamma_{zy} - 3\gamma_{zz}), \\
c_{xz} &= 10(-3\gamma_{xy} + \gamma_{yy} + 3\gamma_{zx} - 3\gamma_{zy}). \quad \text{(B5)}
\end{aligned}
$$

The expectation values of the direction cosine functions $\Phi_{Zx} = -\sin\theta \cos\chi$ and $\Phi_{Zz} = \cos\theta$ and their respective powers and products can be computed by solving the time-dependent rotational dynamics of the system, as described in Sec. II B of the main text. Note that for a linear molecule, the hyperpolarizability tensor reduces to three independent elements γ_{zz}, $\gamma_{xy} = \frac{1}{3}\gamma_{xx} = \frac{1}{3}\gamma_{yy}$, and $\gamma_{xz} = \gamma_{yz}$. In this case, the coefficients a_x, b_{Yx}, b_{Zx}, and c_{xz} are null and Eqs. (7) and (8) of the main text reduce to the expression of the THG field given in Ref. [69].

APPENDIX C: QUANTUM MECHANICAL CALCULATION OF THE LINEAR AND NONLINEAR POLARIZABILITY OF ACETONE

Our approach to the calculation of (hyper)polarizability relies on a computational philosophy presented in sufficient detail in a previous paper [73]. Only a few essential points are expanded here.

The energy of a neutral molecule interacting with a weak, static electric field is given as an expansion [74]

$$
\begin{aligned}
E^p = {} & E^0 - \mu_\alpha E_\alpha - \tfrac{1}{2}\alpha_{\alpha\beta} E_\alpha E_\beta \\
& - \tfrac{1}{6}\beta_{\alpha\beta\gamma} E_\alpha E_\beta E_\gamma - \tfrac{1}{24}\gamma_{\alpha\beta\gamma\delta} E_\alpha E_\beta E_\gamma E_\delta + \cdots, \quad \text{(C1)}
\end{aligned}
$$

where E^0 is the energy of the free molecule and E_α, E_β, ... are the electric field components. The rest of the terms are the permanent properties of the molecule, that is, the dipole moment (μ_α), dipole polarizability ($\alpha_{\alpha\beta}$), first dipole hyperpolarizability ($\beta_{\alpha\beta\gamma}$), and second dipole hyperpolarizability ($\gamma_{\alpha\beta\gamma\delta}$). The subscripts denote Cartesian components.

A repeated subscript implies summation over x, y, and z. The number of independent components is strictly regulated by symmetry. We follow closely Buckingham's conventions and notation. In addition to the Cartesian components of the (hyper)polarizability tensors we calculate also the isotropic components and the anisotropy, defined as

$$\overline{\alpha} = (\alpha_{xx} + \alpha_{yy} + \alpha_{zz})/3,$$

$$\Delta\alpha = \frac{1}{\sqrt{2}}[(\alpha_{xx} - \alpha_{yy})^2 + (\alpha_{yy} - \alpha_{zz})^2 + (\alpha_{zz} - \alpha_{xx})^2]^{1/2},$$

$$\overline{\beta} = \frac{3}{5}(\beta_{xzz} + \beta_{xyy} + \beta_{xxx}),$$

$$\overline{\gamma} = \frac{1}{5}(\gamma_{xxxx} + \gamma_{yyyy} + \gamma_{zzzz} + 2\gamma_{zzyy} + 2\gamma_{yyxx} + 2\gamma_{xxzz}).$$

$$\text{(C2)}$$

All computational efforts in this paper rely on two atom-specific basis sets designed for the electric properties of acetone. Both are built upon a 6-31G substrate, as implemented in the G03 set of codes [75]. Basis A consists of 154 and basis B of 196 CGTF. The additional basis functions are diffuse CGTF or atom-optimized [76,77], or added even-temperedly.

Synoptically:

$$A = \text{6-31G} + 1sp(\text{O})\text{diff} + 6sp(\text{C})\text{diff}$$
$$+ 6s(\text{H})\text{diff} + 2d(\text{C})\text{opt} + 2d(\text{O})\text{opt} + 12p(\text{H})\text{opt}.$$
$$\text{(C3)}$$

Additional polarization functions are added even-temperedly on C, O, H to obtain the B basis:

$$B = A + 1d(\text{O})\text{even-temp}$$
$$+ 3d(\text{C})\text{even-temp} + 6p(\text{H})\text{even-temp}.   \text{(C4)}$$

6D CGTF were used in all cases.

All optimizations and calculations were carried out at the theoretical MP2(FULL)/cc-pvdz [78] geometry. All electrons were correlated in the MP2 geometry calculations. In the finite-field electric property calculations the four innermost MO were kept frozen. All properties are shown in atomic units, unless otherwise specified. Conversion factors to SI units are [79] energy, 1 $E_h = 4.35974434(19) \times 10^{-18}$ J; length, 1 $a_0 = 0.52917721092(17) \times 10^{-10}$ m; dipole moment **I**, 1 $ea_0 = 8.47835326(19) \times 10^{-30}$ Cm; polarizability α, 1 $e^2a^2E^{-1} = 1.6487772754(16) \times 10^{-41}$ $C^2\,m^2\,J^{-1}$; first hyperpolarizability β, 1 $e^3a^3E^{-2} = 3.206361449(71) \times 10^{-53}$ $C^3\,m^3\,J^{-2}$; and second hyperpolarizability γ, 1 $e^4a^4E^{-3} = 6.23538054(28) \times 10^{-65}$ $C^4\,m^4\,J^{-3}$. For simplicity's sake molecular property values are given as pure numbers in the text, i.e., μ/ea_0, $\alpha/e^2a^2E^{-1}$, $\alpha/e^3a^3E^{-2}$, and $\gamma/e^4a^4E^{-3}$.

The calculated electric properties of acetone are given in Table I of the main text. We add here a few pertinent remarks on the (a) stability of our values and (b) the comparison to other selected results.

(a) The SCF dipole moment with basis A is $\mu(A) = -1.3659$. For B we have $\mu(B) = -1.3637$, lower by 1% in absolute terms. At the correlated MP2 level of theory $\mu(A) = -1.1540$ and $\mu(B) = -1.1510$, again lower by 1% in absolute terms. The proximity of the dipole polarizability values is easily verified. For the mean dipole polarizability, the increase from A to B brings about a small increase of the SCF and MP2 values, as $\overline{\alpha}(A) < \overline{\alpha}(B)$ for both theoretical methods. For $\overline{\beta}$, electron correlation reduces significantly the SCF $\overline{\beta}(A)$ and $\overline{\beta}(B)$ values while the basis set effect is small in all cases. For the second hyperpolarizability $\overline{\gamma}$, both SCF dependence and electron correlation effects are significant. Compare $\overline{\gamma}(A) = 4767$ (SCF) to $\overline{\gamma}(B) = 4996$ (SCF) and $\overline{\gamma}(A) = 8153$ (MP2) to $\overline{\gamma}(B) = 8683$ (MP2).

(b) Our best value of the dipole moment of acetone is MP2/B result $\mu = -1.1510$, in excellent agreement with the experimental value of -1.14, as measured by Swalen and Costain [80]. Our dipole polarizability ($\alpha_{\alpha\alpha}$) and first hyperpolarizability ($\beta_{\alpha\beta\gamma}$) values agree quite well with the corresponding SCF/PolX values of Eckart $et\ al.$ [81]. Our SCF/B values for the mean polarizability and first hyperpolarizability are $\overline{\alpha} = 39.8673$ and $\overline{\beta} = 46.66$ to be compared to 38.84 and 46.1, respectively, reported by Eckart $et\ al.$ Last, our SCF/A of the mean $\overline{\gamma} = 4767$ agrees well with the $ab\ initio$ value of Zhou and Dykstra $\overline{\gamma} = 4490$ [82].

[1] R. Velotta, N. Hay, M. B. Mason, M. Castillejo, and J. P. Marangos, High-Order Harmonic Generation in Aligned Molecules, Phys. Rev. Lett. **87**, 183901 (2001).

[2] J. Itatani, D. Zeidler, J. Levesque, M. Spanner, D. M. Villeneuve, and P. B. Corkum, Controlling High Harmonic Generation with Molecular Wave Packets, Phys. Rev. Lett. **94**, 123902 (2005).

[3] L. S. Spector, M. Artamonov, S. Miyabe, T. Martinez, T. Seideman, M. Guehr, and P. H. Bucksbaum, Axis-dependence of molecular high harmonic emission in three dimensions, Nat. Commun. **5**, 3190 (2014).

[4] J. Itatani, J. Levesque, D. Zeidler, H. Niikura, P. B. Corkum, and D. M. Villeneuve, Tomographic imaging of molecular orbitals with high-harmonic generation, Nature **432**, 867 (2004).

[5] C. Vozzi, M. Negro, F. Calegari, G. Sansone, M. Nisoli, S. De Silvestri, and S. Stagira, Generalized molecular orbital tomography, Nat. Phys. **7**, 822 (2011).

[6] S. Ramakrishna and T. Seideman, Intense Laser Alignment in Dissipative Media as a Route to Solvent Dynamics, Phys. Rev. Lett. **95**, 113001 (2005).

[7] H. Zhang, B. Lavorel, F. Billard, J. M. Hartmann, E. Hertz, O. Faucher, J. Ma, J. Wu, E. Gershnabel, Y. Prior, and I. S. Averbukh, Rotational Echoes as a Tool for Investigating Ultrafast Collisional Dynamics of Molecules, Phys. Rev. Lett. **122**, 193401 (2019).

[8] J. Ma, H. Zhang, B. Lavorel, F. Billard, E. Hertz, J. Wu, C. Boulet, J.-M. Hartmann, and O. Faucher, Observing collisions beyond the secular approximation limit, Nat. Commun. **10**, 5780 (2019).

[9] H. Xu, E. Lötstedt, T. Ando, A. Iwasaki, and K. Yamanouchi, Alignment-dependent population inversion in N_2^+ in intense few-cycle laser fields, Phys. Rev. A **96**, 041401(R) (2017).

[10] H. Stapelfeldt and T. Seideman, Colloquium: Aligning molecules with strong laser pulses, Rev. Mod. Phys. **75**, 543 (2003).

[11] C. P. Koch, M. Lemeshko, and D. Sugny, Quantum control of molecular rotation, Rev. Mod. Phys. **91**, 035005 (2019).

[12] K. Lin, I. Tutunnikov, J. Ma, J. Qiang, L. Zhou, O. Faucher, Y. Prior, I. Averbukh, and J. Wu, Spatiotemporal rotational dynamics of laser-driven molecules, Adv. Photonics **2**, 024002 (2020).

[13] P. M. Felker, Rotational coherence spectroscopy: Studies of the geometries of large gas-phase species by picosecond time-domain methods, J. Chem. Phys. **96**, 7844 (1992).

[14] P. M. Felker and A. H. Zewail, Rotational coherence phenomena, in *Jet Spectroscopy and Molecular Dynamics*, edited by J. M. Hollas and D. Phillips (Springer Netherlands, Dordrecht, 1995), pp. 181.

[15] K. F. Lee, D. M. Villeneuve, P. B. Corkum, A. Stolow, and J. G. Underwood, Field-Free Three-Dimensional Alignment of Polyatomic Molecules, Phys. Rev. Lett. **97**, 173001 (2006).

[16] R. Damari, S. Kallush, and S. Fleischer, Rotational Control of Asymmetric Molecules: Dipole- versus Polarizability-Driven Rotational Dynamics, Phys. Rev. Lett. **117**, 103001 (2016).

[17] A. Korobenko and V. Milner, Adiabatic Field-Free Alignment of Asymmetric Top Molecules with an Optical Centrifuge, Phys. Rev. Lett. **116**, 183001 (2016).

[18] I. F. Tenney, M. Artamonov, T. Seideman, and P. H. Bucksbaum, Collisional decoherence and rotational quasirevivals in asymmetric-top molecules, Phys. Rev. A **93**, 013421 (2016).

[19] M. Yoshida, N. Takemoto, and Y. Ohtsuki, Three-dimensional alignment of asymmetric-top molecules induced by polarization-shaped optimal laser pulses, Phys. Rev. A **98**, 053434 (2018).

[20] A. Rouzée, S. Guérin, O. Faucher, and B. Lavorel, Field-free molecular alignment of asymmetric top molecules using elliptically polarized laser pulses, Phys. Rev. A **77**, 043412 (2008).

[21] T. Grohmann and M. Leibscher, Nuclear spin selective alignment of ethylene and analogues, J. Chem. Phys. **134**, 204316 (2011).

[22] J. Mikosch, A. E. Boguslavskiy, I. Wilkinson, M. Spanner, S. Patchkovskii, and A. Stolow, Channel- and Angle-Resolved above Threshold Ionization in the Molecular Frame, Phys. Rev. Lett. **110**, 023004 (2013).

[23] E. Péronne, M. D. Poulsen, C. Z. Bisgaard, H. Stapelfeldt, and T. Seideman, Nonadiabatic Alignment of Asymmetric Top Molecules: Field-Free Alignment of Iodobenzene, Phys. Rev. Lett. **91**, 043003 (2003).

[24] M. D. Poulsen, E. Péronne, H. Stapelfeldt, C. Z. Bisgaard, S. S. Viftrup, E. Hamilton, and T. Seideman, Nonadiabatic alignment of asymmetric top molecules: Rotational revivals, J. Chem. Phys. **121**, 783 (2004).

[25] S. Li, F. Ling, Y. Wang, J. Long, X. Deng, B. Jin, and B. Zhang, Femtosecond-laser-induced nonadiabatic alignment in photoexcited pyrimidine, Phys. Rev. A **96**, 033419 (2017).

[26] J. J. Larsen, K. Hald, N. Bjerre, H. Stapelfeldt, and T. Seideman, Three-Dimensional Alignment of Molecules Using Elliptically Polarized Laser Fields, Phys. Rev. Lett. **85**, 2470 (2000).

[27] S. S. Viftrup, V. Kumarappan, L. Holmegaard, C. Z. Bisgaard, H. Stapelfeldt, M. Artamonov, E. Hamilton, and T. Seideman, Controlling the rotation of asymmetric top molecules by the combination of a long and a short laser pulse, Phys. Rev. A **79**, 023404 (2009).

[28] I. Tutunnikov, E. Gershnabel, S. Gold, and I. S. Averbukh, Selective orientation of chiral molecules by laser fields with twisted polarization, J. Phys. Chem. Lett. **9**, 1105 (2018).

[29] H. Zhang, F. Billard, X. Yu, O. Faucher, and B. Lavorel, Dissipation dynamics of field-free molecular alignment for symmetric-top molecules: Ethane (C_2H_6), J. Chem. Phys. **148**, 124303 (2018).

[30] G. Karras, E. Hertz, F. Billard, B. Lavorel, J. M. Hartmann, O. Faucher, E. Gershnabel, Y. Prior, and I. S. Averbukh, Orientation and Alignment Echoes, Phys. Rev. Lett. **114**, 153601 (2015).

[31] V. V. Ilyushin and J. T. Hougen, A fitting program for molecules with two equivalent methyl tops and C_{2v} point-group symmetry at equilibrium: Application to existing microwave, millimeter, and submillimeter wave measurements of acetone, J. Mol. Spectrosc. **289**, 41 (2013).

[32] P. R. Bunker, *Molecular Symmetry and Spectroscopy*, 1st ed. (Academic Press, New York, 1979).

[33] J. K. G. Watson, Determination of centrifugal distortion coefficients of asymmetric-top molecules, J. Chem. Phys. **46**, 1935 (1967).

[34] J. K. G. Watson, Determination of centrifugal-distortion coefficients of asymmetric-top molecules. II. Dreizler, Dendl, and Rudolph's results, J. Chem. Phys. **48**, 181 (1968).

[35] J. K. G. Watson, Determination of centrifugal distortion coefficients of asymmetric-top molecules. III. Sextic coefficients, J. Chem. Phys. **48**, 4517 (1968).

[36] L. F. Pašteka, M. Melicherčík, P. Neogrády, and M. Urban, CASPT2 and CCSD(T) calculations of dipole moments and polarizabilities of acetone in excited states, Mol. Phys. **110**, 2219 (2012).

[37] M. P. Allen and D. J. Tildesley, *Computer Simulation of Liquids* (Clarendon Press, Oxford, 1987).

[38] M. Ferrario, M. Haughney, I. R. McDonald, and M. L. Klein, Molecular-dynamics simulation of aqueous mixtures: Methanol, acetone, and ammonia, J. Chem. Phys. **93**, 5156 (1990).

[39] L. H. Coudert, F. Billard, E. Hertz, O. Faucher, and B. Lavorel, Torsional control of the methyl group in methanol, Phys. Rev. A **100**, 043425 (2019).

[40] J.-M. Hartmann, C. Boulet, H. Zhang, F. Billard, O. Faucher, and B. Lavorel, Collisional dissipation of the laser-induced alignment of ethane gas: A requantized classical model, J. Chem. Phys. **149**, 154301 (2018).

[41] J. M. Hartmann, J. Ma, T. Delahaye, F. Billard, E. Hertz, J. Wu, B. Lavorel, C. Boulet, and O. Faucher, Molecular alignment echoes probing collision-induced rotational-speed changes, Phys. Rev. Research **2**, 023247 (2020).

[42] J. Ma, H. Zhang, B. Lavorel, F. Billard, J. Wu, C. Boulet, J. M. Hartmann, and O. Faucher, Ultrafast collisional dissipation of symmetric-top molecules probed by rotational alignment echoes, Phys. Rev. A **101**, 043417 (2020).

[43] L. H. Coudert, Optimal control of the orientation and alignment of an asymmetric-top molecule with terahertz and laser pulses, J. Chem. Phys. **148**, 094306 (2018).

[44] A. Rouzée, S. Guérin, V. Boudon, B. Lavorel, and O. Faucher, Field-free one-dimensional alignment of ethylene molecule, Phys. Rev. A **73**, 033418 (2006).

[45] I. C. Bowater, J. M. Brown, and A. Carrington, Microwave spectroscopy of nonlinear free radicals. I. General theory and

application to the Zeeman effect in HCO, Proc. R. Soc. London, Ser. A. **333**, 265 (1973).

[46] X. Ren, V. Makhija, and V. Kumarappan, Multipulse Three-Dimensional Alignment of Asymmetric Top Molecules, Phys. Rev. Lett. **112**, 173602 (2014).

[47] P. M. Felker and A. H. Zewail, Molecular structures from ultrafast coherence spectroscopy, in *Femtosecond Chemistry*, Vol. 1, edited by J. Manz and L. Wöste (VCH, Weinheim, New York, 1995), Chap. 5, p. 193.

[48] L. L. Connell, T. C. Corcoran, P. W. Joireman, and P. M. Felker, Observation and description of a new type of transient in rotational coherence spectroscopy, J. Phys. Chem. **94**, 1229 (1990).

[49] T. Vieillard, F. Chaussard, F. Billard, D. Sugny, O. Faucher, S. Ivanov, J. M. Hartmann, C. Boulet, and B. Lavorel, Field-free molecular alignment for probing collisional relaxation dynamics, Phys. Rev. A **87**, 023409 (2013).

[50] J.-M. Hartmann, C. Boulet, T. Vieillard, F. Chaussard, F. Billard, O. Faucher, and B. Lavorel, Dissipation of alignment in CO_2 gas: A comparison between ab initio predictions and experiments, J. Chem. Phys. **139**, 024306 (2013).

[51] M. T. von Ratzsch, C. Wohlforth, U. Credo, A. Jarmuschewitsch, and U. Nehmer, Dipolmomente und polarisierbarkeiten polarer stoffe ans statischen DK-messungen, Z. Phys. Chem. **257**, 161 (1976).

[52] O. Dorosh and Z. Kisiel, Electric dipole moments of acetone and of acetic acid measured in supersonic expansion, Acta Phys. Pol. A **112**, S95 (2007).

[53] V. Renard, M. Renard, A. Rouzée, S. Guérin, H. R. Jauslin, B. Lavorel, and O. Faucher, Non-intrusive monitoring and quantitative analysis of strong laser field-induced impulsive alignment, Phys. Rev. A **70**, 033420 (2004).

[54] J. M. Hartmann and C. Boulet, Quantum and classical approaches for rotational relaxation and nonresonant laser alignment of linear molecules: A comparison for CO_2 gas in the nonadiabatic regime, J. Chem. Phys. **136**, 184302 (2012).

[55] S. K. Kim, S. Pedersen, and A. H. Zewail, Direct femtosecond observation of the transient intermediate in the α-cleavage reaction of $(CH_3)2CO$ to $2CH_3+CO$: Resolving the issue of concertedness, J. Chem. Phys. **103**, 477 (1995).

[56] J. C. Owrutsky and A. P. Baronavski, Ultrafast photodissociation dynamics of the S1 and S2 states of acetone, J. Chem. Phys. **110**, 11206 (1999).

[57] N. Rusteika, K. B. Moller, and T. I. Solling, New insights on the photodynamics of acetone excited with 253–288 nm femtosecond pulses, Chem. Phys. Lett. **461**, 193 (2008).

[58] Y. Haas, Photochemical α-cleavage of ketones: Revisiting acetone, Photochem. Photobiol. Sci. **3**, 6 (2004).

[59] S. Pabst and R. Santra, Alignment of asymmetric-top molecules using multiple-pulse trains, Phys. Rev. A **81**, 065401 (2010).

[60] S. Pabst and R. Santra, Erratum: Alignment of asymmetric-top molecules using multiple-pulse trains [Phys. Rev. A **81**, 065401 (2010)], Phys. Rev. A **82**, 049901(E) (2010).

[61] D. Rosenberg, R. Damari, S. Kallush, and S. Fleischer, Rotational echoes: Rephasing of centrifugal distortion in laser-induced molecular alignment, J. Phys. Chem. Lett. **8**, 5128 (2017).

[62] G. Karras, E. Hertz, F. Billard, B. Lavorel, G. Siour, J. M. Hartmann, O. Faucher, E. Gershnabel, Y. Prior, and I. S.

Averbukh, Experimental observation of fractional echoes, Phys. Rev. A **94**, 033404 (2016).

[63] B. Wang, L. He, Y. He, Y. Zhang, R. Shao, P. Lan, and P. Lu, All-optical measurement of high-order fractional molecular echoes by high-order harmonic generation, Opt. Express **27**, 30172 (2019).

[64] K. Lin, P. Lu, J. Ma, X. Gong, Q. Song, Q. Ji, W. Zhang, H. Zeng, J. Wu, G. Karras, G. Siour, J.-M. Hartmann, O. Faucher, E. Gershnabel, Y. Prior, and I. S. Averbukh, Echoes in Space and Time, Phys. Rev. X **6**, 041056 (2016).

[65] E. L. Hahn, Spin echoes, Phys. Rev. **80**, 580 (1950).

[66] N. A. Kurnit, I. D. Abella, and S. R. Hartmann, Observation of a Photon Echo, Phys. Rev. Lett. **13**, 567 (1964).

[67] D. Rosenberg, R. Damari, and S. Fleischer, Echo Spectroscopy in Multilevel Quantum-Mechanical Rotors, Phys. Rev. Lett. **121**, 234101 (2018).

[68] J. F. Reintjes, *Nonlinear Optical Parametric Processes in Liquids and Gases*, Vol. 1 (Academic Press, Orlando, 1984), p. 466.

[69] J. Houzet, E. Hertz, F. Billard, B. Lavorel, and O. Faucher, Molecular alignment allows low-order harmonic generation by circular light in a gas, Phys. Rev. A **88**, 023859 (2013).

[70] E. Skantzakis, S. Chatziathanasiou, P. A. Carpeggiani, G. Sansone, A. Nayak, D. Gray, P. Tzallas, D. Charalambidis, E. Hertz, and O. Faucher, Polarization shaping of high-order harmonics in laser-aligned molecules, Sci. Rep. **6**, 39295 (2016).

[71] J. K. G. Watson, Aspects of quartic and sextic centrifugal effects on rotational energy levels, in *Vibrational Spectra and Structure*, Vol. 6 (Elsevier, Amsterdam, 1977), Chap. 1, p. 1.

[72] R. N. Zare, *Angular Momentum: Understanding Spatial Aspects in Chemistry and Physics* (Wiley-Interscience, New York, 1988), p. 349.

[73] G. Maroulis, A systematic study of basis set, electron correlation, and geometry effects on the electric multipole moments, polarizability, and hyperpolarizability of HCl, J. Chem. Phys. **108**, 5432 (1998).

[74] A. D. Buckingham, Permanent and induced molecular moments and long-range intermolecular forces, in *Advances in Chemical Physics* (John Wiley & Sons, New York, 1967), p. 107.

[75] M. J. Frisch, *Gaussian 03, Revision D.01* (Gaussian, Inc., Wallingford, CT, 2004).

[76] G. Maroulis, Static dipole polarizability of N-octane calculated with MinPol basis sets, Comput. Lett. **2**, 139 (2006).

[77] G. Maroulis (unpublished).

[78] Basis cc-pcvdz, as implemented in Gaussian 03.

[79] P. J. Mohr, B. N. Taylor, and D. B. Newell, CODATA recommended values of the fundamental physical constants: 2010, Rev. Mod. Phys. **84**, 1527 (2012).

[80] J. D. Swalen and C. C. Costain, Internal rotation in molecules with two internal rotors: Microwave spectrum of acetone, J. Chem. Phys. **31**, 1562 (1959).

[81] U. Eckart, V. E. Ingamells, M. G. Papadopoulos, and A. J. Sadlej, Vibrational effects on electric properties of cyclopropenone and cyclopropenethione, J. Chem. Phys. **114**, 735 (2001).

[82] T. Zhou and C. E. Dykstra, Additivity and transferability of atomic contributions to molecular second dipole hyperpolarizabilities, J. Chem. Phys. A **104**, 2204 (2000).